ACS Photonics

pubs.acs.org/journal/apchd5

Article

Thermalization and Spin Relaxation Dynamics of Localized Photocarriers in the Band Tails of Nanocrystalline $MAPbBr_3$ Films

Chuang Zhang,[⊥] Paul Bailey,[⊥] Shuchun Zhang,[⊥] Uyen Huynh, Xiaomei Jiang,* Stephen McGill, Dmitry Semenov, and Z. Valy Vardeny*

Cite This: https://doi.org/10.1021/acsphotonics.4c00873

Read Online

ACCESS | Metrics & More | Article Recommendations | Supporting Information

ABSTRACT: We have studied the spin properties of localized photocarriers in the band tails (BT) of polycrystalline $MAPbBr_3$ films having a nanometer crystal size using circularly polarized photoluminescence (PL) induced by a magnetic field up to 17.5 T at cryogenic temperatures as well as time-of-flight (TOF) transient photocurrent. The absorption spectrum of these films reveals BT states caused by structural and energetic disorders, having a broadly distributed Urbach edge ranging from 28 to 120 meV. This is corroborated by dispersive transport of photogenerated electrons and holes observed via TOF, where the photocarriers thermalize with time deeply in the BT, giving rise to time-dependent mobility. Consequently, the PL emission spectrum in these films originates from radiative recombination of the localized electron and hole pairs in the BT states. Upon applying a magnetic field in the Faraday configuration, field-induced circular polarized PL has been observed, from which an effective Landé *g*-factor of the localized e−h pairs, g_{e-h}, was extracted to be 2.5 ± 0.2, in good agreement with the *g*-factor of free excitons measured using magnetic circular dichroism spectroscopy. In addition, we also found that the spin relaxation time for the e−h pairs in the BT states is ∼26 ns at 5 K and ∼10 ns at 80 K, indicating that nanocrystalline $MAPbBr_3$ could be a good candidate for applications in spintronics and quantum computing.

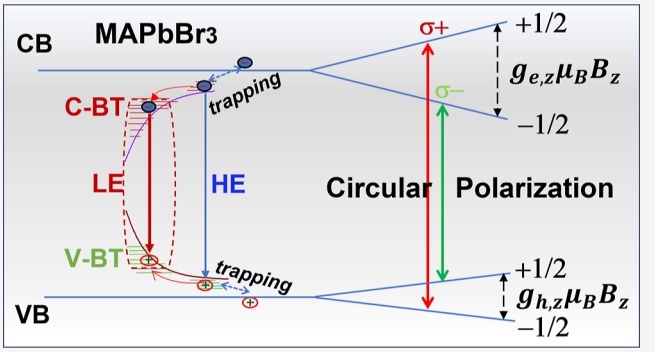

KEYWORDS: *metal halide perovskites, photoluminescence, magnetic field-induced circular polarization, Landé g-factor, electron−hole pair, carrier mobility*

INTRODUCTION

The three-dimensional (3D) hybrid trihalide perovskites are highly sought-after materials for a variety of optoelectronic applications including solar cells,[1−3] photodetectors,[4,5] light-emitting diodes,[6−8] and spintronic devices.[9,10] This class of semiconductors has the general molecular formula of AMX_3, where A is either an organic (such as methylammonium, MA^+) or a metal (i.e., cesium, Cs^+) cation, M is a divalent metal cation such as lead, Pb^{2+}, and X is a halide anion such as Br^-. The crystal structure is composed of eight interconnected MX_6^{4-} octahedrals forming a cubic cage, with A^+ residing in the center of the cage. These materials have versatile optoelectronic properties, such as high absorption that is tunable across the visible solar spectrum, relatively high carrier mobility, and low exciton binding energy which can be tuned via facile solution-based synthesis.[11] Following the high performance of methylammonium lead triiodide ($MAPbI_3$) in photovoltaic devices,[12−15] there has been a large amount of basic research into the structural and optoelectronic properties of other hybrid trihalide perovskites, with the majority of significant contributions listed in a few review papers.[16−18] $MAPbBr_3$ has shown similar properties to $MAPbI_3$, yet a significant difference is its higher bandgap and exciton binding energy.[19−22] As a result, $MAPbBr_3$-based solar cells are less efficient than those based on $MAPbI_3$.[2,3,13] However, the photoluminescence (PL) quantum yield in $MAPbBr_3$ is much stronger than in $MAPbI_3$ which may be due to the tighter bound excitons.[6,23,24] Excitons in $MAPbBr_3$ have been found to play a role as free excitons,[25,26] trapped excitons in subgap states,[27−29] and also as indirect excitons caused by the Rashba spin splitting of the continuum bands.[30] The weight of various exciton types is highly dependent on sample preparation and experimental conditions.[31]

A continuous energy distribution of trap states near the band edge, known as band tail (BT) states, is common in disordered semiconductors.[32,33] BT states that result from structural disorder and strains along the crystal grain boundaries have

Received: May 14, 2024
Revised: October 2, 2024
Accepted: October 3, 2024

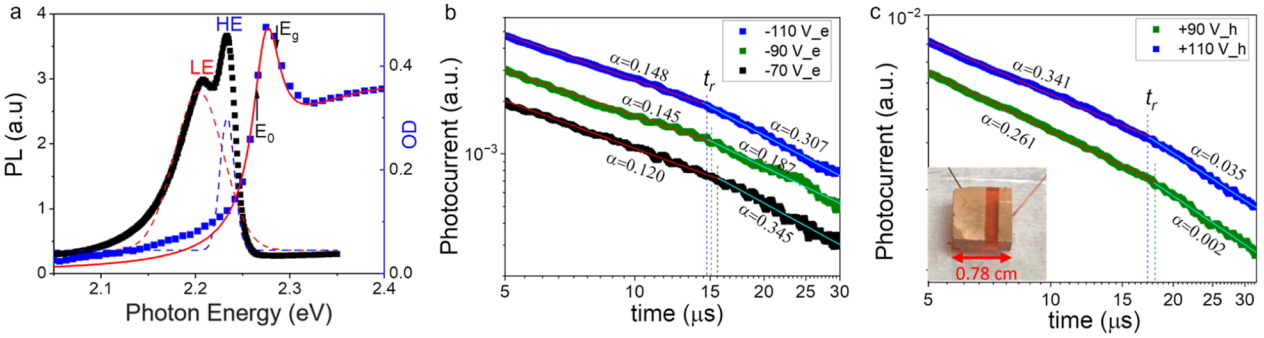

Figure 1. (a) Absorption (blue squares) and photoluminescence (PL, black squares) spectra of a nanocrystalline $MAPbBr_3$ film (grain size <100 nm) measured at 45 K. The solid red line through the data points is a fit using the Elliot model (eq S1), whereas the broken color lines are Gauss fits of the two PL components' spectra. Transport properties of electrons (b) and holes (c) in the $MAPbBr_3$ crystal measured by time-of-flight (TOF) photocurrent at various applied DC voltages, plotted on a double logarithmical scale. The fits (broken lines) are a power-law decay using eq 1, in which the dispersion parameter, α, is extracted, as noted. The transit time (indicated by thin broken lines), t_r, is found in each case at the intersection between the two power-law decays. The inset in (c) shows a single-crystal device used in the TOF measurements.

been reported in hybrid lead trihalide perovskites such as $MAPbI_3$ and $MAPbBr_3$.[27,29,34] BT states below the mobility edge have been shown to be effective traps for photocarriers, and radiative recombination from excitons trapped in BT states has been reported in several trihalide perovskites.[27,29] Meanwhile, the observation of the Urbach tail in the absorption of the polycrystalline film reflects the disordered nature of the system that results from structural disorders and compositional deficiency, as well as local disorders at grain boundaries and surfaces.[21,27,34] PL emission spectroscopy is a popular method for studying excitons. In particular, the PL of $MAPbBr_3$ has been extensively studied in various sample morphologies including bulk single crystals, polycrystalline films, and nanocrystals, with main contributions summarized in a recent review article.[22]

It is worth mentioning that the exciton binding energy in $MAPbBr_3$ polycrystalline films was found to span a wide range from 17 to 80 meV, depending on samples and experimental techniques.[22] Since the exciton binding energy is larger than the thermal activation energy at cryogenic temperature, the PL emission in $MAPbBr_3$ has been attributed to excitons including those trapped in BT states.[26−28] In this work, however, we show that in nanocrystalline $MAPbBr_3$ films, the energetic disorder results in an Urbach edge with energy of comparable value to the exciton binding energy. As a result, the PL emission in these films originates from radiative recombination of the localized electron−hole pairs rather than from excitons. We found that the PL lifetime is ∼1 ns for the electron and hole (e−h) pair in shallow traps and ∼7.5 ns for the e−h pairs in deeper traps in BT. Furthermore, dispersive transport properties for both electrons and holes have been observed, confirming the existence of BT states in $MAPbBr_3$.

Strong spin-orbital coupling (SOC) in $MAPbBr_3$ has led to many spin-related phenomena such as Rashba splitting,[35,36] magnetic field effect,[25,37−39] and inverse spin hall effect.[36] Magnetic field-induced circular polarization (FICPO) is a well-suited experimental tool to study the spin-dependent optical transitions in semiconductors.[40,41] When an external magnetic field lifts the spin degeneracy via Zeeman splitting, circularly polarized absorption,[38] reflection, and emission are usually observed.[25,37] FICPO in PL emission has been reported in $MAPbI_3$, where the PL is dominant by band-to-band free electron and hole recombination.[42] Also, FICPO in reflection was measured in a high-quality $MAPbBr_3$ single crystal where free exciton emission dominated, and a Landé g-factor was extracted to be 2.6.[25] In the present work, we study the magneto-optical properties of electrons and holes localized in BT states. We have observed strong field-induced circularly polarized PL in the nanocrystalline $MAPbBr_3$ film. By measuring the degree of circular polarization, P_c, as a function of magnetic field and sample temperature, we extract the effective Landé g-factor g_{eff} to be 2.5 ± 0.2 for the localized e−h pair, in agreement with the g_{eff} for the free exciton measured by magnetic-induced circular dichroism.[38] The agreement confirms that g_{eff} is not affected by the localization of photocarriers in the BT states. Moreover, we also found that the localized e−h pairs have a relatively long spin relaxation time of over 20 ns at cryogen temperature and in a high magnetic field (17.5 T), which is substantially longer than that of the free electrons and holes in $MAPbBr_3$ single crystals (ps to sub-ns),[38,45,55] as well as excitons in micrometer crystalline $MAPbBr_3$ films.[43,44] This implies that $MAPbBr_3$ with an ultrasmall grain size may be a good candidate for applications in spintronics and quantum computing.

RESULTS AND DISCUSSION

Figure 1a shows the absorption (blue square) and PL (black square) spectra of a nanocrystalline $MAPbBr_3$ film (grain size < 100 nm, Figure S6) measured at T = 45 K . The absorption spectrum exhibits a long rising tail, with a sharp exciton peak at 2.27 eV followed by continuum band absorption. Since both excitonic and continuum band transitions contribute to the absorption, the spectrum was fit using the Elliot model[46] (solid red line) in order to obtain more accurate values of the optical bandgap (E_g) and 1 s free exciton energy (E_0); see Figure S3 for details. From the fitting, we extract E_g = 2.285 eV and the exciton binding energy E_b = 20 meV in the nanocrystalline film. From these values, we obtain $E_0 = E_g - E_b$ to be 2.265 eV. These values are consistent with previous reports of $MAPbBr_3$ films.[21,47] A long Urbach tail is visibly present, seen as the deviation from the Elliot fit. Fitting this tail using the standard BT formula $\alpha = \alpha_0 e^{(E-E_g)/E_u}$ yields the Urbach tail energy, E_u (see Supporting Information Section 3 for details). There is a broad distribution of E_u in this small crystalline domain sample, ranging from 28 to 120 meV. The extracted E_u is much larger than previously reported in a $MAPbBr_3$ film with a larger crystal domain.[43] Such a large E_u agrees with the disordered nature of the film, consistent with the band tail (BT) states

https://doi.org/10.1021/acsphotonics.4c00873
ACS Photonics XXXX, XXX, XXX−XXX

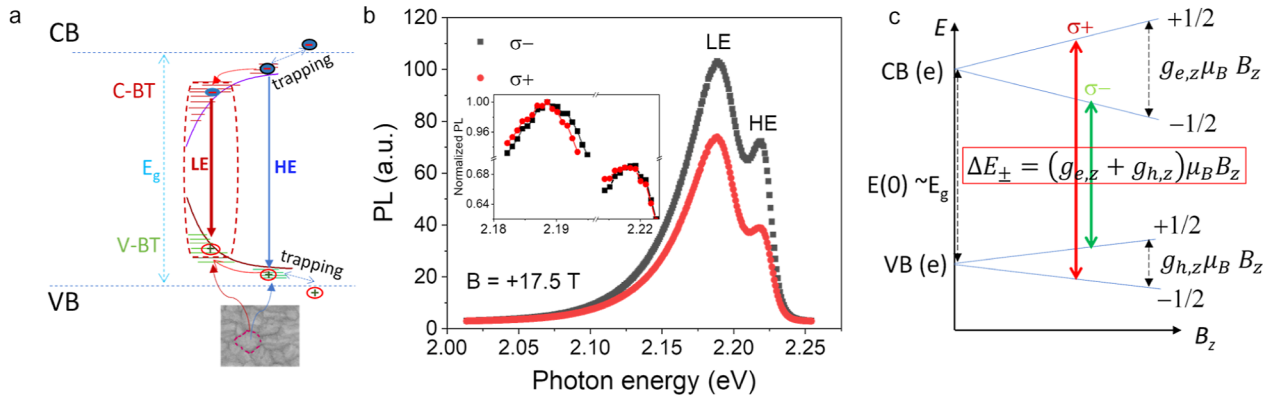

Figure 2. (a) Schematic drawing that describes the PL emission from recombination of electron−hole pairs trapped at various depths of the conduction and valence band tails (C-BT/V-BT). The red arrows in the C-BT and V-BT indicate photocarrier thermalization that results in the HE to LE bands, respectively. The bottom inset is a SEM image of the $MAPbBr_3$ film where the HE emission is from the nanometer-size crystallites, whereas the LE band is from the grain boundaries. (b) Field-induced circularly polarized PL of the $MAPbBr_3$ film at T = 5 K in a magnetic field B = 17.5 T normal to the film (Faraday geometry). The right (σ^+)/left (σ^-) circularly polarized PL is shown as red/black symbols. The inset shows the small shift of the LE and HE peaks at the two emission helicities. (c) Selection rules for the optical transitions of the trapped electron and hole pair, where the two allowed transitions are marked in red/green for right (σ^+) and left (σ^-) circularly polarized emission, respectively. $\Delta E_\pm$ is the Zeeman splitting between σ^+/σ^- emission photon energies.

formed by energetic and structural disorders near the band edge in another hybrid lead iodide perovskite.[29]

The disorder in the $MAPbBr_3$ film is corroborated by the dispersive transport characteristics of photocarriers measured by time-of-flight (TOF) photocurrent (PC) transient as seen in Figure 1b,c. Instead of a constant PC(t) until the photocarriers arrive at the opposite electrodes, we monitor a power-law decay for both photogenerated electrons and holes. The transit time, t_r, is found from the intersection between the two PC decay regimes.[48] The solid lines are fitted using the standard Scher and Montroll formula[49] given by

$$I(t) = I_0 t^{-(1-\alpha)} \text{ for } t < t_r \text{ and } I_0 t^{-(1+\alpha)} \text{ for } t > t_r \quad (1)$$

where I_0 is a constant and α (<1) is the dispersive parameter, which is lower for cases with increased disorder. It is worth mentioning that the PC(t) decays even though the e−h recombination is essentially suppressed in the TOF configuration, an approximation that is usually used for the TOF measurements for $d \gg 1/\alpha_0$, where d is the sample thickness and α_0 is the absorption coefficient at the laser excitation wavelength. Consequently, the suppressed e−h recombination is due to the constant external electric field applied in the device driving the electrons and holes to opposite directions. Hence, the decay is due to the photocarrier thermalization to deeper BT states that possess smaller mobility. Usually, α before and after the transit time is identical; however, it is not what we observe here. The deviation was previously found in amorphous systems such as π-conjugated polymers,[48] an indication that the distribution of charge transport sites does not follow a purely exponential function. The important point is that α < 1 in our case, which clearly shows the dispersive nature of carrier transport in the $MAPbBr_3$ crystal, reflecting the disorder in the sample. The charge drift mobility can be determined by

$$\mu = \frac{d}{t_r F} = \frac{d^2}{t_r V} \quad (2)$$

From the TOF results, we extracted an average mobility $\bar{\mu}_e$ = 23 $cm^2/V.s$ for the electrons and $\bar{\mu}_h$ = 18 $cm^2/V\,s$ for the holes. These values are close to that of a single crystal[50] and larger than a polycrystalline sample.[51] We observed that both μ_e and μ_h have an inverse dependence on the applied voltage. We speculate that this might be due to ion (particularly the halide ion) migration, which is common in halide perovskites.[52,53] Ion migration is accelerated at higher voltage; hence, the effective electric field is reduced, and that explains the decrease of carriers' mobility with the applied voltage. A more thorough investigation of transport properties in $MAPbBr_3$ is beyond the scope of this work and will be presented in a separate report. The relevant point here is that both hole and electron mobilities in the $MAPbBr_3$ crystal are dispersive due to the abundance of BT states close to the continuum bands; we believe that this is true also in our nanocrystalline $MAPbBr_3$ film. Table S1 summarizes the fitting results.

The steady state PL spectrum of the $MAPbBr_3$ film (Figure 1a) shows a dual-band feature, with a high-energy (HE) band at 2.233 eV and a broader low-energy (LE) band at 2.208 eV having a long tail toward the red. The asymmetric shape of the LE band indicates that it contains more than one source. The large Stokes shift of ~30 meV between the HE band and the free 1s exciton, E_0, extracted from the Elliot fit (see Supporting Information Section 3) indicates that the cw PL here is unlikely to arise from recombination of free excitons.[25] The dependence of the PL on the laser excitation intensity confirms that the radiative recombination involves trapped carriers (Figure S6). Furthermore, the LE band is much broader than the HE band and has a dominant contribution to the PL spectrum at T < 50 K (see Figure S5). This indicates that LE and HE bands are not related by a phonon replica. The dual-band PL emission spectrum was previously observed in both single-crystal and polycrystalline $MAPbBr_3$ samples;[25,26,28,30,31,37,43,54,55] yet there is no consensus about its origin. A few scenarios were offered, including transitions from a direct bandgap and indirect bandgap due to Rashba splitting,[30,55] recombination of free and trapped excitons at surface states,[28] free exciton and trapped exciton at band-tail states,[27,29] and phonon replica,[56] just to name a few. In our nanocrystalline $MAPbBr_3$ film, multiple grain boundaries and

https://doi.org/10.1021/acsphotonics.4c00873
ACS Photonics XXXX, XXX, XXX−XXX

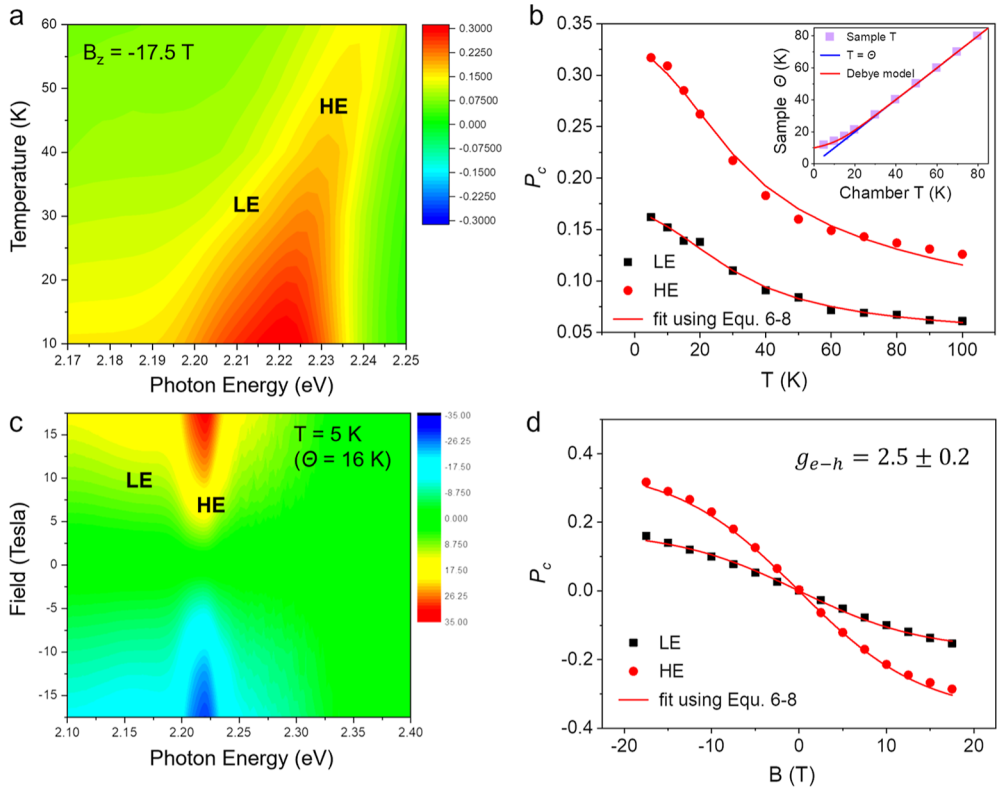

Figure 3. False-color 2D contour plot of the degree of FICPO spectrum, $P_c(B_z,T,E)$, calculated using eq 4, at (a) various cryochamber temperatures at B_z = −17.5 T and (c) various B_z at cryochamber temperature T = 5 K. (b) P_c of the LE band (black squares) and HE band (red circles) as a function of the cryochamber temperature T, at B_z = −17.5 T. The inset shows the sample temperature, Θ at different chamber temperatures T according to eq 5. (d) P_c of the HE and LE bands as a function of B_z at T = 5 K. The lines through the data points are fits using eqs 5−7 in the text.

vast surface densities introduce disorder in the film. With an Urbach energy of 28−120 meV that exceeds the exciton binding energy (∼20 meV), electrons and holes trapped within the BT states do not form excitons at low temperatures. We thus believe that the PL observed here primarily comes from recombination of electron and hole (e−h) pairs trapped in their respective BT states. Since both LE and HE bands are present in "polycrystalline" and "single crystal" samples (see Figure S4), we believe that the sharper band (HE) is due to recombination of e−h pairs at shallow BT states intrinsic to the crystalline bulk phase, whereas the broader band (LE) originates from deeply trapped e−h pair recombination associated with the grain boundaries and surfaces. We further elaborate that the LE band is not from a presumed indirect transition caused by the Rashba splitting previously observed in $MAPbBr_3$ single crystals,[30,55] mainly due to two reasons: (1) the reported red shift of the indirect peak in the single crystal sample is opposite to what is observed with the LE band here, which shows a blue shift with increasing temperature (see Figure S5); (2) the reported energy separation between the dual LE−HE bands (∼40 meV) is much larger than that observed here (∼18 meV) at 77 K. Further verification is provided by a recent theoretical calculation,[57] which shows that the Rashba splitting in $MAPbBr_3$ is observable in the orthorhombic phase (low temperature) only in the (001) plane, which is shown to be parallel to the substrate in our film sample, proven by the out-of-plane XRD (see Figure S6c). With the incident light normal to the Rashba plane (along the Z direction), no Rashba splitting is expected due to the broken symmetry in the XOY plane. Figure 2a presents a schematic illustration of the PL in the nanocrystalline film.

Having identified the origin of LE and HE emission bands, we turn to their optical properties in a magnetic field to further study the spin-dependent optical transitions. For this, we applied an external magnetic field B_z normal to the film plane, i.e., in the Faraday configuration. The steady-state PL emission was collected along the z-direction after passing a quarter wave plate (QWP) parallel to the film plane (Figure S1 for the experimental setup). Figure 2b shows the PL measured at T = 5 K and B_z = 17.5 T, recorded at left (i.e., polarization vector σ+, with angular momentum J_z = +1) and right (i.e., polarization vector σ^-, with angular momentum J_z = −1) circular polarizations, respectively. The FICPO of the PL is clearly observed, where the spectra are $PL(\sigma^+) \neq PL(\sigma^-)$. Note that in $MAPbBr_3$, the electron at the bottom of the conduction band has its total spin angular momentum J_e = 1/2 with z projection of J_{ez} = ±1/2, whereas the hole at the top of the valence band has its total spin momentum S_h = 1/2 with a z projection of S_{hz} = ±1/2.[58] In the simple picture of bimolecular recombination, the σ^- (σ^+) polarized PL originates from the recombination between electrons with J_{ez} = +(−)1/2 and holes with S_{hz} = +(−)1/2 spin states, which should satisfy the conservation of total angular momentum, J_z = + (−)1, and the Zeeman splitting of optical transition is the summation of the Zeeman splitting of the initial and final spin states as schematically shown in Figure 2.[58] In this case

$$\Delta E_{\pm} = (g_{e,z} + g_{h,z})\mu_B B_z = g_{eff,z}\mu_B B_z \quad (3)$$

Hence, the effective Landé g-factor of the e−h pair, g_{e-h}, equals to the sum of that of electrons and holes (i.e., $g_{eff,z} = g_{e,z} + g_{h,z}$). Our recent measurements have shown that $g_{e,z}$ = 1.83 and $g_{h,z}$

https://doi.org/10.1021/acsphotonics.4c00873
ACS Photonics XXXX, XXX, XXX−XXX

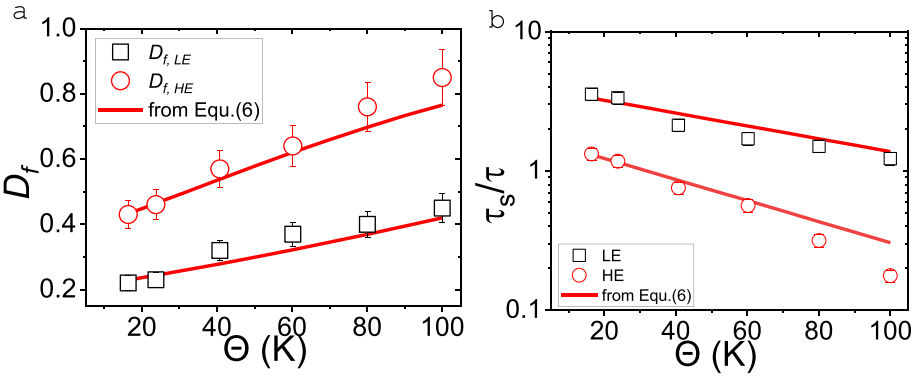

Figure 4. (a) Reducing factor, D_f dependence on sample temperature, Θ, for the LE (black square) and HE bands (red circle). (b) Ratio of the spin relaxation time (τ_s) over the PL lifetime (τ) extracted from (a). The solid line is simulated from eq 7, and the symbol represents data obtained from $P_c(B_z)$ measured at different temperatures (see Supporting Information Section 8 for details).

= 0.55 in the $MAPbBr_3$ film in the Faraday geometry; thus, $g_{eff,z} = g_{e,z} + g_{h,z} = 2.38$.[38]

Due to the broad nature of the LE and HE bands in the PL spectrum (with fwhm of 15−30 meV), it is rather difficult to accurately obtain the Zeeman splitting ($\Delta E_{\pm}$) from the peak energy shift with B_z (see the inset of Figure 2b). Therefore, we cannot directly obtain the PL-related g-factor based on eq 3. Instead, we used an alternative method to extract the g-factor of the emissive species. We derive the induced circularly polarized photoluminescence (i.e., FICPO) spectrum via the degree of circular polarization, P_c, as a function of magnetic field B_z, cryochamber temperature, T, and photon energy E

$$P_c(B_z, T, E) = \frac{PL(\sigma^+) - PL(\sigma^-)}{PL(\sigma^+) + PL(\sigma^-)} \tag{4}$$

Figure 3a shows the 2D contour plot of the P_c spectral dependence on the cryochamber temperatures from 5 K to 60 K. The P_c spectrum is dominated by a sharp peak (HE) accompanied by a broad shoulder (LE). Accompanying the reduced magnitude of P_c, a continuous blue shift of the FICPO spectrum with increasing temperature is seen, similar to the PL spectrum presented in Figure S5.

Due to the laser-induced heating, the sample temperature, Θ, under excitation is higher than the measured cryochamber temperature, T. The deviation of Θ from T is especially acute at very low temperatures where the film's specific heat is very small (see the inset of Figure 3b). For instance, Θ = 16 K when T = 5 K (see eq 5).

At constant laser power, the sample temperature Θ is related to the chamber temperature T by[59]

$$\Theta = T + a\Theta^{-3} \tag{5}$$

when considering that the sample heat capacity is proportional to Θ^3, following the Debye law at low temperatures. Therefore, we will use the sample temperature Θ rather than the cryochamber T in our discussion below.

At steady-state conditions, $P_c(B_z,\Theta)$ is determined by the difference in populations of the σ^+ and σ^- spin sublevels, assuming the same radiative transition rate for both, subject to a Boltzmann distribution at B_z and temperature Θ.[59] However, as previously shown in $MAPbI_3$,[60] thermal equilibrium of the photogenerated e−h spins is not completely reached within the e−h pair lifetime due to the competition between spin relaxation time, τ_s, and the e−h pair lifetime, τ. In this case, a reducing factor $D_f(\Theta) = \tau/(\tau + \tau_s)$ is introduced to the Boltzmann statistics formula (eq 6) to account for the loss of polarization due to non-equilibrium conditions. It has been shown that τ_s/τ decays exponentially with the sample temperature at a fixed magnetic field.[42] We can then express $D_f(\Theta)$

$$D_f(\Theta) = \frac{\tau}{\tau + \tau_s} = \frac{1}{1 + \frac{\tau_s}{\tau}} = \frac{1}{1 + p_2 e^{-p_1\Theta}} \tag{6}$$

where p_1 and p_2 are functions of magnetic field B_z; this is understandable since τ_s in eq 6 is field-dependent.[38] Consequently, $P_c(B_z,\Theta)$ is described by a modified Brillouin function[42]

$$P_c(B_z, \Theta) = \left(\frac{e^{-\frac{\Delta E}{k_B\Theta}} - 1}{e^{-\frac{\Delta E}{k_B\Theta}} + 1}\right) D_f(\Theta) = \left(\tanh \frac{-g_{eff,z}\mu_B B_z}{2k_B\Theta}\right) D_f(\Theta) \tag{7}$$

where k_B is the Boltzmann constant, μ_B is the Bohr magneton, and $\Delta E = E(J_{z=+1}) - E(J_{z=-1})$ is the energy difference between the two Zeeman-split states ($=g_{eff,z}\mu_B B_z$), where $g_{eff,z}$ is the effective Landé g-factor of the e−h pairs.

In Figure 3b, we plot P_c dependence on cryochamber temperature T for the LE and HE PL bands at B_z = −17.5 T. The solid line through the data points is the best fit of $P_c(T)$ using eqs 5−7, with four parameters: a, p_1, p_2, and $g_{eff,z}$. From the fitting, we extract $g_{eff,z}$ = 2.43 ± 0.2 for the LE band and $g_{eff,z}$ = 2.56 ± 0.2 for the HE band. The extracted $g_{eff,z}$ or g_{e-h} for the e−h pairs is in agreement with $g_{eff,z}$ for free excitons measured by magnetically induced circular dichroism,[38] confirming that $g_{eff,z}$ is not affected by the localization of e−h in BT states. The fit is good up to T = 80 K. We speculate that this may be due to the phase transition from orthorhombic I to II previously reported in $MAPbBr_3$ crystals.[61] Table S3 gives the details of the fitting parameters.

We also measured circularly polarized PL dependence on the magnetic field B_z at a fixed temperature. Figure 3c shows the 2D contour plot of the FICPO P_c spectrum at various magnetic field strengths at T = 5 K (where Θ = 16 K). A clear peak at ∼2.22 eV is from the HE band, whereas a broad shoulder at ∼2.16 eV is from the LE band. The slight blue shift of the maxima in the FICPO spectrum compared with the relevant peaks in the PL spectrum is the result of the spin splitting between σ^- and σ^+ emissions.[42] In Figure 3d, we plot

https://doi.org/10.1021/acsphotonics.4c00873
ACS Photonics XXXX, XXX, XXX−XXX

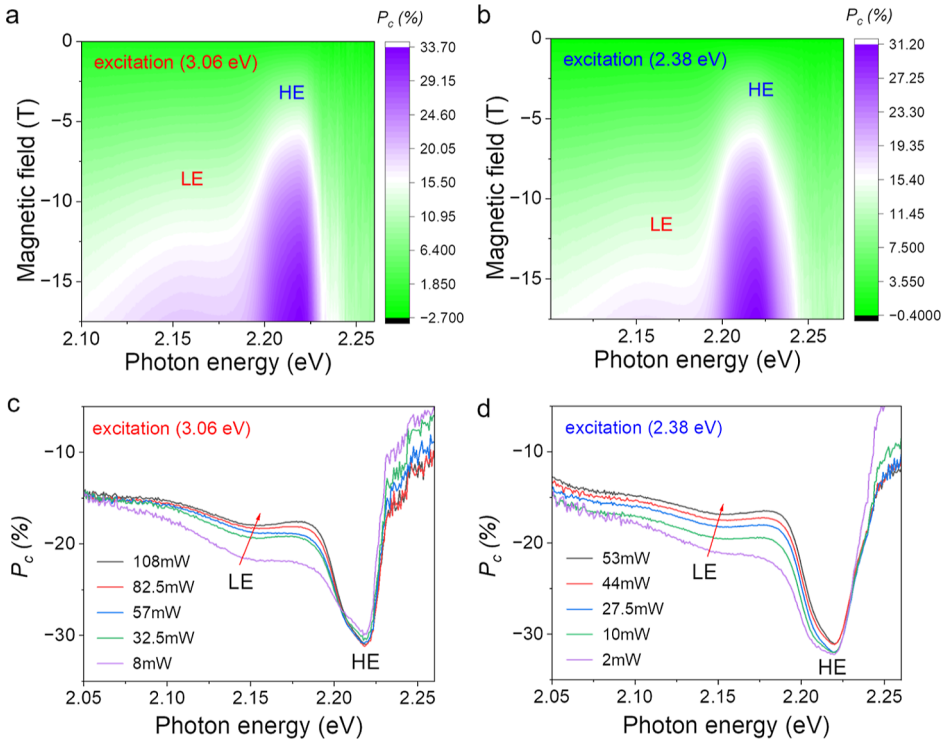

Figure 5. False-color 2D contour plot of the FICPO (or P_c) spectrum at various magnetic field strengths, with a laser excitation photon energy of (a) 3.06 eV (power 8 mW) and (b) 2.38 eV (power 2 mW). FICPO spectrum at B_z = 17.5 T varying with excitation power at an excitation energy of 3.06 eV (c) and 2.38 eV (d). The red arrow indicates the red shift of the LE peak with increasing laser power.

$P_c(B_z)$ at Θ = 16 K. Very good fits of $P_c(B_z)$ for both LE and HE bands are achieved using the g-factors obtained from $P_c(T)$ fitting in Figure 3b, respectively, with $D_{f,LE}$ = 0.22 and $D_{f,HE}$ = 0.43. By measuring $P_c(B_z)$ at different sample temperatures Θ (see Supporting Information Section 8), we can obtain the temperature dependence of $D_f(\Theta)$ and compare that with the calculated $D_f(\Theta)$ from eq 6. Such a comparison is shown in Figure 4a. A very good agreement is seen between the two sets of experimental data, i.e., $P_c(T)$ and $P_c(B_z)$. D_f increases with sample temperature, which is to be expected since the spin relaxation time τ_s decreases with increasing temperature, as shown in Figure S8d. Similarly, Figure 4b plots the values of τ_s/τ (symbols) obtained from $P_c(B_z)$ at different temperatures (see Supporting Information Section 8), as compared with the calculated values from eq 6. Clearly, τ_s/τ follows an exponential decay with sample temperature, confirming the validity of eq 6.

We also measured the recombination lifetime, τ, using time-resolved PL in a similar polycrystalline film (see Supporting Information Section 7) and obtained $\tau_{LE} \sim 1.3$ ns and $\tau_{HE} \sim 7.5$ ns at T = 6 K. We obtained $D_f < 1$ for both LE and HE bands up to 100 K, as shown in Figure 4a. This indicates that spin equilibrium is not reached for the localized e−h pairs before recombination sets in. Based on eq 6 at T = 5 K (Θ = 16 K), we estimate the spin relaxation time $\tau_{s,HE} \sim 2$ ns for the e−h pair localized at the shallow BT states that give rise to the HE band and $\tau_{s,e-h3} \sim 27$ ns for e−h pairs trapped in the deep BT states related to the LE emission (Figure 2a). The spin relaxation time (τ_s) dependence on temperature for both bands is shown in Figure S8d. It is seen that τ_s decreases with the temperature and is similar for both LE and HE bands, indicating their shared origin, namely, BT states.

Figure 5a,b shows the field dependence of the FICPO (or P_c) spectrum at different laser excitation energies at T = 5 K. Even though the photogenerated electrons and holes have much larger kinetic energy upon absorption of the higher energy photons, there is a minimal difference in FICPO between the two excitation regimes. This shows that the spin orientation is robust against excess energy. While the energy relaxation of electrons and holes into the BT states is fast, their spin relaxation is much slower due to the suppression of the Dyakonov−Perel (D−P) mechanism,[62] as observed in semiconductor quantum dots.[63,64] Our $MAPbBr_3$ film has a nanometer-size domain, where the photocarriers are naturally confined, similar to the case in quantum dots. In fact, numerous reports have shown that the D−P mechanism is strongly suppressed in solution-based metal halide perovskites, evidenced by carrier spin coherence time of the order of nanoseconds.[65−67] Considering the small size of the crystal domains and abundance of grain boundaries in our film, we believe that the Elliot−Yafet (E−Y) mechanism is responsible for exciton spin relaxation, which occurs via scattering over the domain boundaries and e−ph interaction.[68] It was previously shown that the e−ph interaction is enhanced due to carrier localization in $CsPbBr_3$.[69] In our case, since the e−h pair in the LE band covers a broader distribution of BT states and is more delocalized (due to much larger E_u), the e−ph coupling is suppressed, resulting in much larger spin relaxation time than that of the HE band. As a matter of fact, the spin relaxation time (few ns to tens of ns at cryogenic temperature) in our nanocrystalline sample is much larger than previously reported in single-crystal samples[45,58] and in polycrystalline films with larger domain sizes,[43,44] supporting our conclusion that the e−h pair in the broad BT states is responsible for the magneto-photoluminescence results. Figure 5c,d presents the FICPO

https://doi.org/10.1021/acsphotonics.4c00873
ACS Photonics XXXX, XXX, XXX−XXX

(or P_c) spectra at B = 17.5 T varying with excitation power at corresponding excitation energies. At both excitation energies, the P_c of the LE band decreases with power. Furthermore, the spectral center of LE shifted to blue as the excitation power increased. This is due to the band-filling which pushes the emission to higher BT states. A previous report has shown that the PL of localized exciton in $MAPbBr_3$ decays faster (τ smaller) at higher emission energy.[27] A smaller τ results in a larger D_{fl} which explains the reduced P_c at higher excitation power. On the other hand, P_c of the HE band shows no change with increasing power at a 3.06 eV excitation yet has a slight reduction and blue shift with increasing power at a 2.38 eV excitation. HE originates from the top of BT states which are filled first even at low excitation intensity, especially with the 3.06 eV excitation, when free carriers are generated.

CONCLUSIONS

In nanocrystalline $MAPbBr_3$ films, where the structural and energetic disorder is substantial, BT states with a continuous energy distribution are formed beneath the optical band gap. These have been revealed by the dispersive transport of the transient TOF photocurrent. Upon photoexcitation under these conditions, the photogenerated electrons and holes are quickly localized in their respective BT states. The PL spectrum at low temperatures reveals two bands, namely, LE and HE, separated by a few tens of meV, both of which originate from recombination of e−h pairs trapped in deep and shallow band tail states, respectively. At a temperature lower than 80 K, the PL lifetime of the deeply localized LE band (∼7.5 ns) is much longer than that of the shallow localized HE band (∼1.3 ns). In the Faraday configuration with a magnetic field normal to the film, FICPO, i.e., the difference between PL (σ^+) and PL (σ^-), has been observed. Fit of the degree of circular polarization (P_c) dependence on the magnetic field and temperature with a modified Brillouin function yields an effective Landé g-factor g_{eff} = 2.5 ± 0.2 for LE and HE bands, in good agreement with g_{eff} = 2.38 for free excitons reported earlier. This shows that the g-factor is not affected by carrier localization. We also found that the spin relaxation time for the deeply localized e−h pairs is over 26 ns at 5 K and over 10 ns at 80 K. The relatively long spin relaxation time in the nanocrystalline $MAPbBr_3$ film may be due to suppression of spin dephasing in the D−P mechanism and e−ph interaction in the E−T mechanism; the two dominant spin relaxation mechanisms in single crystals of metal halide perovskites.

ASSOCIATED CONTENT

Supporting Information

The Supporting Information is available free of charge at https://pubs.acs.org/doi/10.1021/acsphotonics.4c00873.

Additional experimental details, materials, and methods, including a schematic drawing of the experimental setup; sample preparation and experimental methods; SEM images of the nanocrystalline film and micrometer-size single crystal; Elliot fitting of the absorption spectrum and the Urbach tail; low-temperature PL dependence on crystalline size; PL dependence on temperature; low-temperature PL dependence on the excitation intensity; electron−hole pair lifetime measured by time-resolved photoluminescence (TRPL); and field-induced circular polarization of PL (FICPO) temperature dependence (PDF)

AUTHOR INFORMATION

Corresponding Authors

Xiaomei Jiang − *Department of Physics, University of South Florida, Tampa, Florida 33620, United States;* orcid.org/0000-0003-4669-6069; Email: xjiang@usf.edu

Z. Valy Vardeny − *Department of Physics & Astronomy, University of Utah, Salt Lake City, Utah 84112, United States;* orcid.org/0000-0002-2298-398X; Email: valy_vardeny@yahoo.com

Authors

Chuang Zhang − *Department of Physics & Astronomy, University of Utah, Salt Lake City, Utah 84112, United States; Beijing National Laboratory for Molecular Sciences, Institute of Chemistry, Chinese Academy of Sciences, Beijing 100190, China;* orcid.org/0000-0003-3709-8294

Paul Bailey − *Department of Physics & Astronomy, University of Utah, Salt Lake City, Utah 84112, United States*

Shuchun Zhang − *Beijing National Laboratory for Molecular Sciences, Institute of Chemistry, Chinese Academy of Sciences, Beijing 100190, China*

Uyen Huynh − *Department of Physics & Astronomy, University of Utah, Salt Lake City, Utah 84112, United States*

Stephen McGill − *National High Magnetic Field Laboratory, Tallahassee, Florida 32310, United States*

Dmitry Semenov − *National High Magnetic Field Laboratory, Tallahassee, Florida 32310, United States*

Complete contact information is available at: https://pubs.acs.org/10.1021/acsphotonics.4c00873

Author Contributions

⊥C.Z., P.B., and S.Z. contributed equally.

Funding

We thank Dr. Peter C. Sercel for helpful discussions. The spectroscopic measurements, the $MAPbBr_3$ film growth, and the theoretical modeling were supported by the Center for Hybrid Organic−Inorganic Semiconductors for Energy (CHOISE), an Energy Frontier Research Center funded by the Office of Basic Energy Sciences, Office of Science within the US Department of Energy through contract number DE-AC36-08G028308. The high-magnetic-field measurements were supported by the Department of Energy Office of Science, Grant DESC0014579. The manuscript write-up was supported by National Science Foundation grant DMR 2054169. The transient photoluminescence measurements were supported by the National Natural Science Foundation of China (grant no. 22090021).

Notes

The authors declare no competing financial interest.

REFERENCES

(1) Noel, N. K.; Wenger, B.; Habisreutinger, S. N.; Patel, J. B.; Crothers, T.; Wang, Z.; Nicholas, R. J.; Johnston, M. B.; Herz, L. M.; Snaith, H. J. Highly Crystalline Methylammonium Lead Tribromide Perovskite Films for Efficient Photovoltaic Devices. *ACS Energy Lett.* **2018**, *3*, 1233−1240.

(2) Heo, J. H.; Song, D. H.; Im, S. H. Planar $CH_3NH_3PbBr_3$ Hybrid Solar Cells with 10.4% Power Conversion Efficiency, Fabricated by Controlled Crystallization in the Spin-Coating Process. *Adv. Mater.* **2014**, *26*, 8179−8183.

(3) Jeyakumar, R.; Bag, A. Methylammonium lead bromide based planar perovskite solar cells using various electron transport layers. *Sol. Energy* **2021**, *221*, 456−467.
(4) Xu, Z.; Zeng, Y.; Meng, F.; Gao, S.; Fan, S.; Liu, Y.; Zhang, Y.; Wageh, S.; Al-Ghamdi, A. A.; Xiao, J.; et al. A High-Performance Self-Powered Photodetector Based on $MAPbBr_3$ Single Crystal Thin Film/MoS_2 Vertical Van Der Waals Heterostructure. *Adv. Mater. Interfaces* **2022**, *9*, 2200912.
(5) Li, S.-X.; Xu, Y.-S.; Li, C.-L.; Guo, Q.; Wang, G.; Xia, H.; Fang, H.-H.; Shen, L.; Sun, H.-B. Perovskite Single-Crystal Microwire-Array Photodetectors with Performance Stability beyond 1 Year. *Adv. Mater.* **2020**, *32*, 2001998.
(6) Tan, Z.-K.; Moghaddam, R. S.; Lai, M. L.; Docampo, P.; Higler, R.; Deschler, F.; Price, M.; Sadhanala, A.; Pazos, L. M.; Credgington, D.; et al. Bright light-emitting diodes based on organometal halide perovskite. *Nat. Nanotechnol.* **2014**, *9*, 687−692.
(7) Prakasam, V.; Tordera, D.; Bolink, H. J.; Gelinck, G. Degradation Mechanisms in Organic Lead Halide Perovskite Light-Emitting Diodes. *Adv. Optical Mater.* **2019**, *7*, 1900902.
(8) Bade, S. G. R.; Li, J.; Shan, X.; Ling, Y.; Tian, Y.; Dilbeck, T.; Besara, T.; Geske, T.; Gao, H.; Ma, B.; et al. Fully Printed Halide Perovskite Light-Emitting Diodes with Silver Nanowire Electrodes. *ACS Nano* **2016**, *10*, 1795−1801.
(9) Wang, J.; Zhang, C.; Liu, H.; McLaughlin, R.; Zhai, Y.; Vardeny, S. R.; Liu, X.; McGill, S.; Semenov, D.; Guo, H.; et al. Spin-optoelectronic devices based on hybrid organic-inorganic trihalide perovskites. *Nat. Commun.* **2019**, *10*, 129.
(10) Sun, D.; Zhang, C.; Kavand, M.; Wang, J.; Malissa, H.; Liu, H.; Popli, H.; Singh, J.; Vardeny, S. R.; Zhang, W.; et al. Surface-enhanced spin current to charge current conversion efficiency in $CH_3NH_3PbBr_3$-based devices. *J. Chem. Phys.* **2019**, *151*, 174709.
(11) Mitzi, D. B. Solution-processed inorganic semiconductors. *J. Mater. Chem.* **2004**, *14*, 2355−2365.
(12) Zhang, W.; Anaya, M.; Lozano, G.; Calvo, M. E.; Johnston, M. B.; Míguez, H.; Snaith, H. J. Highly Efficient Perovskite Solar Cells with Tunable Structural Color. *Nano Lett.* **2015**, *15*, 1698−1702.
(13) Bush, K. A.; Palmstrom, A. F.; Yu, Z. J.; Boccard, M.; Cheacharoen, R.; Mailoa, J. P.; McMeekin, D. P.; Hoye, R. L. Z.; Bailie, C. D.; Leijtens, T.; et al. 23.6%-efficient monolithic perovskite/silicon tandem solar cells with improved stability. *Nat. Energy* **2017**, *2*, 17009.
(14) Zuo, C.; Bolink, H. J.; Han, H.; Huang, J.; Cahen, D.; Ding, L. Advances in Perovskite Solar Cells. *Adv. Sci.* **2016**, *3*, 1500324.
(15) Huang, J.; Yuan, Y.; Shao, Y.; Yan, Y. Understanding the physical properties of hybrid perovskites for photovoltaic applications. *Nat. Rev. Mater.* **2017**, *2*, 17042.
(16) Saba, M. Rule-breaking perovskites. *Nature* **2018**, *553*, 163−164.
(17) Peng, J.; Chen, Y.; Zheng, K.; Pullerits, T.; Liang, Z. Insights into charge carrier dynamics in organo-metal halide perovskites: from neat films to solar cells. *Chem. Soc. Rev.* **2017**, *46*, 5714−5729.
(18) Chen, X.; Lu, H.; Yang, Y.; Beard, M. C. Excitonic Effects in Methylammonium Lead Halide Perovskites. *J. Phys. Chem. Lett.* **2018**, *9*, 2595−2603.
(19) Tanaka, K.; Takahashi, T.; Ban, T.; Kondo, T.; Uchida, K.; Miura, N. Comparative study on the excitons in lead-halide-based perovskite-type crystals $CH_3NH_3PbBr_3$ $CH_3NH_3PbI_3$. *Solid State Commun.* **2003**, *127*, 619−623.
(20) Galkowski, K.; Mitioglu, A.; Miyata, A.; Plochocka, P.; Portugall, O.; Eperon, G. E.; Wang, J. T.-W.; Stergiopoulos, T.; Stranks, S. D.; Snaith, H. J.; et al. Determination of the exciton binding energy and effective masses for methylammonium and formamidinium lead tri-halide perovskite semiconductors. *Energy Environ. Sci.* **2016**, *9*, 962−970.
(21) Wenger, B.; Nayak, P. K.; Wen, X.; Kesava, S. V.; Noel, N. K.; Snaith, H. J. Consolidation of the optoelectronic properties of $CH_3NH_3PbBr_3$ perovskite single crystals. *Nat. Commun.* **2017**, *8*, 590.
(22) Droseros, N.; Tsokkou, D.; Banerji, N. Photophysics of Methylammonium Lead Tribromide Perovskite: Free Carriers, Excitons, and Sub-Bandgap States. *Adv. Energy Mater.* **2020**, *10*, 1903258.
(23) Lafalce, E.; Zhang, C.; Zhai, Y.; Sun, D.; Vardeny, Z. V. Enhanced emissive and lasing characteristics of nano-crystalline MAPbBr3 films grown via anti-solvent precipitation. *J. Appl. Phys.* **2016**, *120*, 143101.
(24) Droseros, N.; Longo, G.; Brauer, J. C.; Sessolo, M.; Bolink, H. J.; Banerji, N. Origin of the Enhanced Photoluminescence Quantum Yield in $MAPbBr_3$ Perovskite with Reduced Crystal Size. *ACS Energy Lett.* **2018**, *3*, 1458−1466.
(25) Baranowski, M.; Galkowski, K.; Surrente, A.; Urban, J.; Kłopotowski, Ł.; Maćkowski, S.; Maude, D. K.; Ben Aich, R.; Boujdaria, K.; Chamarro, M.; et al. Giant Fine Structure Splitting of the Bright Exciton in a Bulk $MAPbBr_3$ Single Crystal. *Nano Lett.* **2019**, *19*, 7054−7061.
(26) Tilchin, J.; Dirin, D. N.; Maikov, G. I.; Sashchiuk, A.; Kovalenko, M. V.; Lifshitz, E. Hydrogen-like Wannier-Mott Excitons in Single Crystal of Methylammonium Lead Bromide Perovskite. *ACS Nano* **2016**, *10*, 6363−6371.
(27) He, H.; Yu, Q.; Li, H.; Li, J.; Si, J.; Jin, Y.; Wang, N.; Wang, J.; He, J.; Wang, X.; et al. Exciton localization in solution-processed organolead trihalide perovskites. *Nat. Commun.* **2016**, *7*, 10896.
(28) Guo, D.; Bartesaghi, D.; Wei, H.; Hutter, E. M.; Huang, J.; Savenije, T. J. Photoluminescence from Radiative Surface States and Excitons in Methylammonium Lead Bromide Perovskites. *J. Phys. Chem. Lett.* **2017**, *8*, 4258−4263.
(29) Wright, A. D.; Milot, R. L.; Eperon, G. E.; Snaith, H. J.; Johnston, M. B.; Herz, L. M. Band-Tail Recombination in Hybrid Lead Iodide Perovskite. *Adv. Funct. Mater.* **2017**, *27*, 1700860.
(30) Ryu, H.; Park, D. Y.; McCall, K. M.; Byun, H. R.; Lee, Y.; Kim, T. J.; Jeong, M. S.; Kim, J.; Kanatzidis, M. G.; Jang, J. I. Static Rashba Effect by Surface Reconstruction and Photon Recycling in the Dynamic Indirect Gap of $APbBr_3$ (A = Cs, CH_3NH_3) Single Crystals. *J. Am. Chem. Soc.* **2020**, *142*, 21059−21067.
(31) Chuliá-Jordán, R.; Juarez-Perez, E. J. Short Photoluminescence Lifetimes Linked to Crystallite Dimensions, Connectivity, and Perovskite Crystal Phases. *J. Phys. Chem. C* **2022**, *126*, 3466−3474.
(32) Engemann, D.; Fischer, R. Photoluminescence in amorphous silicon. *Phys. Status Solidi B* **1977**, *79*, 195−202.
(33) Yamaguchi, A.; Tada, T.; Ninomiya, T. Time-Resolved Spectroscopy of Photoluminescence in Hydrogenated Amorphous Silicon. *J. Phys. Soc. Jpn.* **1993**, *62*, 332−339.
(34) Ni, Z.; Bao, C.; Liu, Y.; Jiang, Q.; Wu, W.-Q.; Chen, S.; Dai, X.; Chen, B.; Hartweg, B.; Yu, Z.; et al. Resolving spatial and energetic distributions of trap states in metal halide perovskite solar cells. *Science* **2020**, *367*, 1352−1358.
(35) Niesner, D.; Wilhelm, M.; Levchuk, I.; Osvet, A.; Shrestha, S.; Batentschuk, M.; Brabec, C.; Fauster, T. Giant Rashba Splitting in CH3NH3PbBr3 Organic-Inorganic Perovskite. *Phys. Rev. Lett.* **2016**, *117*, 126401.
(36) Huang, Z.; Vardeny, S. R.; Wang, T.; Ahmad, Z.; Chanana, A.; Vetter, E.; Yang, S.; Liu, X.; Galli, G.; Amassian, A.; et al. Observation of spatially resolved Rashba states on the surface of $CH_3NH_3PbBr_3$ single crystals. *Appl. Phys. Rev.* **2021**, *8*, 031408.
(37) Kostadinov-Mutzafi, A.; Tilchin, J.; Shapiro, A.; Dirin, D. N.; Kovalenko, M. V.; Tan, L. Z.; Lifshitz, E. Impact of anisotropy in spin-orbit coupling on the magneto-optical properties of bulk lead halide perovskites. *Phys. Rev. B* **2022**, *106*, 035303.
(38) Huynh, U. N.; Bodin, R.; Pan, X.; Bailey, P.; Liu, H.; McGill, S.; Semenov, D.; Sercel, P. C.; Vardeny, Z. V. Magneto-optical studies of hybrid organic/inorganic perovskite: The case of methyl-ammonium lead bromide. *Phys. Rev. B* **2024**, *109*, 014316.
(39) Kirstein, E.; Yakovlev, D. R.; Glazov, M. M.; Zhukov, E. A.; Kudlacik, D.; Kalitukha, I. V.; Sapega, V. F.; Dimitriev, G. S.; Semina, M. A.; Nestoklon, M. O.; et al. The Landé factors of electrons and holes in lead halide perovskites: universal dependence on the band gap. *Nat. Commun.* **2022**, *13*, 3062.
(40) Furis, M.; Htoon, H.; Petruska, M. A.; Klimov, V. I.; Barrick, T.; Crooker, S. A. Bright-exciton fine structure and anisotropic

https://doi.org/10.1021/acsphotonics.4c00873
ACS Photonics XXXX, XXX, XXX−XXX

exchange in CdSe nanocrystal quantum dots. *Phys. Rev. B* **2006**, *73*, 241313.
(41) Hirasawa, M.; Ishihara, T.; Goto, T.; Uchida, K.; Miura, N. Magnetoabsorption of the lowest exciton in perovskite-type compound (CH_3NH_3)PbI_3. *Physica B* **1994**, *201*, 427−430.
(42) Zhang, C.; Sun, D.; Yu, Z.-G.; Sheng, C.-X.; McGill, S.; Semenov, D.; Vardeny, Z. V. Field-induced spin splitting and anomalous photoluminescence circular polarization in $CH_3NH_3PbI_3$ films at high magnetic field. *Phys. Rev. B* **2018**, *97*, 134412.
(43) Wang, R.; Hu, S.; Yang, X.; Yan, X.; Li, H.; Sheng, C. Circularly polarized photoluminescence and Hanle effect measurements of spin relaxation in organic−inorganic hybrid perovskite films. *J. Mater. Chem. C* **2018**, *6*, 2989−2995.
(44) Zhou, M.; Sarmiento, J. S.; Fei, C.; Zhang, X.; Wang, H. Effect of Composition on the Spin Relaxation of Lead Halide Perovskites. *J. Phys. Chem. Lett.* **2020**, *11*, 1502−1507.
(45) Zhao, W.; Su, R.; Huang, Y.; Wu, J.; Fong, C. F.; Feng, J.; Xiong, Q. Transient circular dichroism and exciton spin dynamics in all-inorganic halide perovskites. *Nat. Commun.* **2020**, *11*, 5665.
(46) Yang, Y.; Ostrowski, D. P.; France, R. M.; Zhu, K.; van de Lagemaat, J.; Luther, J. M.; Beard, M. C. Observation of a hot-phonon bottleneck in lead-iodide perovskites. *Nat. Photonics* **2016**, *10*, 53−59.
(47) Comin, R.; Walters, G.; Thibau, E. S.; Voznyy, O.; Lu, Z.-H.; Sargent, E. H. Structural, optical, and electronic studies of wide-bandgap lead halide perovskites. *J. Mater. Chem. C* **2015**, *3* (34), 8839−8843.
(48) Mozer, A. J.; Sariciftci, N. S.; Pivrikas, A.; Österbacka, R.; Juška, G.; Brassat, L.; Bässler, H. Charge carrier mobility in regioregular poly(3-hexylthiophene) probed by transient conductivity techniques: A comparative study. *Phys. Rev. B* **2005**, *71*, 035214.
(49) Scher, H.; Montroll, E. W. Anomalous transit-time dispersion in amorphous solids. *Phys. Rev. B* **1975**, *12*, 2455−2477.
(50) Musiienko, A.; Pipek, J.; Praus, P.; Brynza, M.; Belas, E.; Dryzhakov, B.; Du, M.-H.; Ahmadi, M.; Grill, R. Deciphering the effect of traps on electronic charge transport properties of methylammonium lead tribromide perovskite. *Sci. Adv.* **2020**, *6*, No. eabb6393.
(51) Emin, S.; Pavlica, E.; Okuyucu, H.; Valant, M.; Bratina, G. Charge carrier transport in polycrystalline $CH_3NH_3PbI_3$ perovskite thin films in a lateral direction characterized by time-of-flight photoconductivity. *Mater. Chem. Phys.* **2018**, *220*, 182−189.
(52) Calado, P.; Telford, A. M.; Bryant, D.; Li, X.; Nelson, J.; O'Regan, B. C.; Barnes, P. R. F. Evidence for ion migration in hybrid perovskite solar cells with minimal hysteresis. *Nat. Commun.* **2016**, *7*, 13831.
(53) McGovern, L.; Futscher, M. H.; Muscarella, L. A.; Ehrler, B. Understanding the Stability of MAPbBr3 versus MAPbI3: Suppression of Methylammonium Migration and Reduction of Halide Migration. *J. Phys. Chem. Lett.* **2020**, *11*, 7127−7132.
(54) Steele, J. A.; Puech, P.; Monserrat, B.; Wu, B.; Yang, R. X.; Kirchartz, T.; Yuan, H.; Fleury, G.; Giovanni, D.; Fron, E.; et al. Role of Electron−Phonon Coupling in the Thermal Evolution of Bulk Rashba-Like Spin-Split Lead Halide Perovskites Exhibiting Dual-Band Photoluminescence. *ACS Energy Lett.* **2019**, *4*, 2205−2212.
(55) Wu, B.; Yuan, H.; Xu, Q.; Steele, J. A.; Giovanni, D.; Puech, P.; Fu, J.; Ng, Y. F.; Jamaludin, N. F.; Solanki, A.; et al. Indirect tail states formation by thermal-induced polar fluctuations in halide perovskites. *Nat. Commun.* **2019**, *10*, 484.
(56) Wright, A. D.; Verdi, C.; Milot, R. L.; Eperon, G. E.; Pérez-Osorio, M. A.; Snaith, H. J.; Giustino, F.; Johnston, M. B.; Herz, L. M. Electron−phonon coupling in hybrid lead halide perovskites. *Nat. Commun.* **2016**, *7*, 11755.
(57) Feng, Q.; Nan, G. Impacts of Crystalline Phases on Rashba Splitting in Lead Halide Perovskites from Bulk to Surfaces. *J. Phys. Chem. C* **2023**, *127*, 16304−16311.
(58) Huynh, U. N.; Liu, Y.; Chanana, A.; Khanal, D. R.; Sercel, P. C.; Huang, J.; Vardeny, Z. V. Transient quantum beatings of trions in hybrid organic tri-iodine perovskite single crystal. *Nat. Commun.* **2022**, *13*, 1428.
(59) Zhang, C.; Sun, D.; Sheng, C. X.; Zhai, Y. X.; Mielczarek, K.; Zakhidov, A.; Vardeny, Z. V. Magnetic field effects in hybrid perovskite devices. *Nat. Phys.* **2015**, *11*, 427−434.
(60) Yu, Z. G. Effective-mass model and magneto-optical properties in hybrid perovskites. *Sci. Rep.* **2016**, *6*, 28576.
(61) Wang, K.-H.; Li, L.-C.; Shellaiah, M.; Wen Sun, K. Structural and Photophysical Properties of Methylammonium Lead Tribromide ($MAPbBr_3$) Single Crystals. *Sci. Rep.* **2017**, *7*, 13643.
(62) Dyakonov, M. I. *Spin Physics in Semiconductors*; Springer, 2017.
(63) Merkulov, I. A.; Efros, A. L.; Rosen, M. Electron spin relaxation by nuclei in semiconductor quantum dots. *Phys. Rev. B* **2002**, *65*, 205309.
(64) Braun, P. F.; Marie, X.; Lombez, L.; Urbaszek, B.; Amand, T.; Renucci, P.; Kalevich, V. K.; Kavokin, K. V.; Krebs, O.; Voisin, P.; et al. Direct Observation of the Electron Spin Relaxation Induced by Nuclei in Quantum Dots. *Phys. Rev. Lett.* **2005**, *94*, 116601.
(65) Odenthal, P.; Talmadge, W.; Gundlach, N.; Wang, R.; Zhang, C.; Sun, D.; Yu, Z.-G.; Valy Vardeny, Z.; Li, Y. S. Spin-polarized exciton quantum beating in hybrid organic−inorganic perovskites. *Nat. Phys.* **2017**, *13*, 894−899.
(66) Yu, Z.-G.; Li, Y. S. Unraveling the Spin Relaxation Mechanism in Hybrid Organic−Inorganic Perovskites. *J. Phys. Chem. C* **2019**, *123*, 14701−14706.
(67) Belykh, V. V.; Yakovlev, D. R.; Glazov, M. M.; Grigoryev, P. S.; Hussain, M.; Rautert, J.; Dirin, D. N.; Kovalenko, M. V.; Bayer, M. Coherent spin dynamics of electrons and holes in $CsPbBr_3$ perovskite crystals. *Nat. Commun.* **2019**, *10*, 673.
(68) Žutić, I.; Fabian, J.; Das Sarma, S. Spintronics: Fundamentals and applications. *Rev. Mod. Phys.* **2004**, *76*, 323−410.
(69) Iaru, C. M.; Brodu, A.; van Hoof, N. J. J.; ter Huurne, S. E. T.; Buhot, J.; Montanarella, F.; Buhbut, S.; Christianen, P. C. M.; Vanmaekelbergh, D.; de Mello Donega, C.; et al. Fröhlich interaction dominated by a single phonon mode in $CsPbBr_3$. *Nat. Commun.* **2021**, *12*, 5844.

https://doi.org/10.1021/acsphotonics.4c00873
ACS Photonics XXXX, XXX, XXX−XXX